

Non-adiabatic electronic relaxation of tetracene from its brightest singlet excited state

A. Scognamiglio,^{1,*} K. S. Thalmann,^{1,*} S. Hartweg,^{1,†,*} N. Rendler,¹ L. Bruder,¹ P. B. Coto,² M. Thoss,¹ and F. Stienkemeier¹

¹University of Freiburg, Institute of Physics, Hermann-Herder-Str. 3, Freiburg, Germany.

²Materials Physics Center (CFM), CSIC and Donostia International Physics Center (DIPC),

Paseo Manuel de Lardizabal 5, 20018 Donostia - San Sebastián, Spain

(Dated: 17.04.2024)

The ultrafast relaxation dynamics of tetracene following UV excitation to a bright singlet state S_6 has been studied with time-resolved photoelectron spectroscopy. With the help of high-level *ab-initio* multireference perturbation theory calculations, we assign photoelectron signals to intermediate dark electronic states S_3 , S_4 and S_5 as well as to a low-lying electronic state S_2 . The energetic structure of these dark states has not been determined experimentally previously. The time-dependent photoelectron yields assigned to the states S_6 , S_5 and S_4 have been analyzed and reveal the depopulation of S_6 within 50 fs, while S_5 and S_4 are populated with delays of about 50 and 80 fs. The dynamics of the lower-lying states S_3 and S_2 seem to agree with a delayed population coinciding with the depopulation of the higher-lying states S_4 - S_6 , but could not be elucidated in full detail due to the low signal levels of the corresponding two-photon ionization probe processes.

I. INTRODUCTION

Polyacenes, a class of polyaromatic hydrocarbons (PAH) consisting of linearly fused benzene rings, currently receive scientific attention from two different fields. While on the one hand they are promising candidates for organic semiconductor and optoelectronic applications[1–3], they are on the other hand, like other PAH also relevant for astrochemistry and astrophysics[4–6]. Research on polyacene semiconductor applications, including transistors[7], flexible displays[8] and photovoltaics[9] focuses on their bulk or thin film properties, like charge carrier mobility and ability to undergo singlet fission, i.e. the ability to produce two excited triplet states after the initial excitation of a singlet exciton. The progress made with these applications may hide the fact that our understanding of the fundamental molecular properties remains incomplete. Fundamental studies of these properties, and how intermolecular interactions affect them [10–13] can provide deep physical insights into relevant mechanisms for application-guided designs. In astrophysics and astrochemistry the interest in PAH stems from their role as carriers of diffuse interstellar bands in the IR region[4], as well as from their importance as reservoir and source of carbon atoms in the interstellar space. Due to these aspects research focuses on IR spectroscopic studies[14–16] and interactions of PAH with radiation in the UV to XUV range present in the interstellar medium and contributing to ionization and dissociation of these species [17].

From an experimental point of view, most previous spectroscopic studies of tetracene have focused on the bright transition to the lowest electronically excited state and its pronounced vibrational progression[18, 19]. Few studies extend far into the UV region of the electromagnetic spectrum, such that the much brighter optical transitions lying in this region have only been studied in crystals, solutions[20] and hot molecular vapors[21], offering only limited spectral res-

olution. Recently, a spectrum of parts of the intense absorption feature recorded with a picosecond laser system has been published[11], but without providing spectral assignments. The electronic structure, composed of few bright states and many dark states has however been studied theoretically[22–46]. Detailed benchmarking of these calculations against experiments was so far not possible, since most of the calculated states could not be observed experimentally. Also the application of high levels of theory for such large molecules remains challenging. Concerning single-photon XUV photoelectron spectroscopy, spectra of tetracene and other polyacenes have been measured[47–50] obtaining the vibronic structure of the tetracene cation.

Only a handful of studies are dedicated to the investigation of non-adiabatic relaxations in neutral PAH excited to high-lying singlet states. Noble *et al.*[51] have investigated the non-adiabatic relaxation of pyrene upon excitation to the third singlet excited state S_3 accessible with a UV photon, revealing consecutive relaxation processes involving several electronic states and various timescales. Radloff *et al.*[52] have studied the ultrafast internal conversion in benzene and its dimer from the excited S_2 state to the S_1 and S_0 states. Blanchet *et al.*[53] report a two-color pump-probe experiment in azulene, where a monoexponential decay of several tens of picoseconds is attributed to the relaxation from the S_4 state to the S_2 and to the ground state via highly excited vibrational states. Further femtosecond photoionization studies of PAH including acenes[54–56] have revealed peculiarities in the ionization mechanisms, including the emission of quasi-thermal electrons, caused by the rapid heating of the electronic subsystem of such molecules, with much slower equilibration with nuclear degrees of freedom. Coronene[40] as well as azulene and naphthalene[57] have been studied with femtosecond photoelectron spectroscopy, revealing the energetic structure of Rydberg states and their sensitivity to the molecular species. Internal conversion between highly excited valence states, Rydberg states and super excited states seem ubiquitous in aromatic molecules[53, 57–59] and the mixing between states with valence and Rydberg character influences the non-adiabatic dynamics in various systems [60]. The conversion of highly excited states of polyacenes

* These authors contributed equally to this work.

† sebastian.hartweg@physik.uni-freiburg.de

to low-lying ones has been recently modelled with a computational approach combining density functional theory and trajectory surface hopping calculations [61, 62]. In this article we present an experimental time-resolved photoelectron spectroscopy study of the relaxation of the tetracene molecule excited to a bright state in the UV, supported by high-level *ab-initio* multireference perturbation theory calculations. The electronic relaxation of highly excited electronic states of isolated molecules is a potential pathway to produce vibrationally hot ground state molecules, and may be considered a necessary stepping stone in the understanding of similar relaxation processes in aggregates and clusters of such molecules, including singlet fission processes.

II. METHODS

A. Experimental

Most aspects of the experimental setup for femtosecond time-resolved photoelectron velocity map imaging (VMI) used in this study have been described previously [63]. An effusive molecular beam of tetracene was produced by a radiatively heated oven at 135°C. The tetracene molecules were excited and ionized by consecutive femtosecond laser pulses intersecting the effusive beam at a right angle in the ionization region of a VMI spectrometer. The femtosecond laser pulses, centered around 400 (VIS) and 267 nm (UV) were created by collinear second and third harmonic (SH, TH) generation of 1.7 W of the output of a regenerative titanium-sapphire amplifier (Coherent Legend, 5 kHz, 2.5 W, 125 fs). The two colors were separated from each other and the remaining fundamental, before the TH pulse was delayed on a variable delay stage. The power of each color was adjusted with a $\lambda/2$ plate and polarizer, with the polarizer setting the horizontal polarization, i.e. parallel to the molecular beam axis and perpendicular to the extraction axis of the VMI spectrometer. Both colors were focused into the interaction region of the VMI spectrometer with individual lenses (focal length 75 mm) and overlapped collinearly using a dichroic mirror. The beam profile at the focal point was measured with a camera to be Gaussian with a beam diameter of 40 μm for the TH and 55 μm for the SH. With these values we obtain intensities between 2.5 and $3 \cdot 10^{11} \text{ W cm}^{-2}$, for a UV power of 2.5 mW, and between 3 and $3.5 \cdot 10^{11} \text{ W cm}^{-2}$, for a VIS power of 5 mW. The obtained photoelectron images were reconstructed following published procedures to obtain photoelectron spectra[64]. For the time-resolved two-color photoelectron spectra the VIS and UV single color photoelectron spectra were subtracted, as was an additional weak 400 nm pump 267 nm probe signal. The latter feature was determined at long negative delays (VIS before UV) and assumed to show a transient signal level described by an error function with a width determined by an estimated cross-correlation of 200 fs (FWHM, see Supplementary Material) for details on the background subtraction).

B. Computational

For the characterization of the electronic spectra of tetracene and its radical cation first we have obtained the equilibrium structures enforcing D_{2h} symmetry, using density functional theory (DFT) with the B3LYP exchange-correlation functional[65–69], and a def2-TZVP basis set[70]. Dispersion interaction corrections were applied following the DFT-D3 method of Grimme *et al.*[71] with Becke-Johnson damping[72]. A frequency analysis was carried out to ensure that the equilibrium structure is a minimum on the potential energy surface. The calculations described above were carried out with the Turbomole V7.5 package[73].

The vertical excitation energies of the neutral tetracene and its radical cation were calculated employing the CASPT2/CASSCF level of theory[74, 75]. The reference wave functions in D_{2h} symmetry were obtained using 15 roots equal weights state-average (SA) CASSCF calculations with an active space of 16 electrons and 16 π -like orbitals employing an ANO-L-VTZP basis set[76–79] (selected after calibration, see supplementary material for further details). The CASPT2 calculations were carried out using an imaginary shift of 0.05 au[80] to mitigate the impact of intruder states. An IPEA shift of 0.25 au was used for the zero order Hamiltonian[81]. The oscillator strengths were calculated using the CASSCF transition dipole moments and the CASPT2 energies.

In addition, the Dyson orbitals were calculated, as described in ref. [82], using the overlap equation:

$$\phi_{IF}^d(x_1) = \sqrt{N} \int \Psi_F^{N-1}(x_2, \dots, x_N) \Psi_I^N(x_1, x_2, \dots, x_N) dx_2 \dots dx_N \quad (1)$$

with the initial and final wavefunctions Ψ_I^N and Ψ_F^{N-1} of the N-electron system and its cation, respectively. These calculations were carried out using MOLCAS 8.4[83] and OpenMOLCAS v20.10[84].

III. RESULTS AND DISCUSSION

A. Single-color and two-color photoelectron spectra

Figure 1 a) depicts a single-color photoelectron spectrum recorded with a UV femtosecond laser pulse centered around 267 nm. The spectrum shows a structured plateau region between 1.5 and 2.5 eV electron kinetic energy and a broad unstructured band below electron energies of 1 eV. The feature at the highest electron kinetic energy of 2.3 eV (label A) is in agreement with direct two-photon ionization ($2 \times 4.64 \text{ eV}$) to the cationic ground state (IP 6.97 eV[49]) while the onset of the low energy feature at around 0.9 eV is in agreement with two-photon ionization to the first two electronically excited cationic states, both located at 8.41 eV[47–49, 85].

The photoelectron spectra obtained by overlapping both laser pulses (UV and VIS) in the ionization region are depicted in figure 1 b) for a delay $\tau \approx 0 \text{ fs}$. The same features that are observed on the structured plateau of figure 1 a) (labels A-D) are visible in the two-color photoelectron spectra,

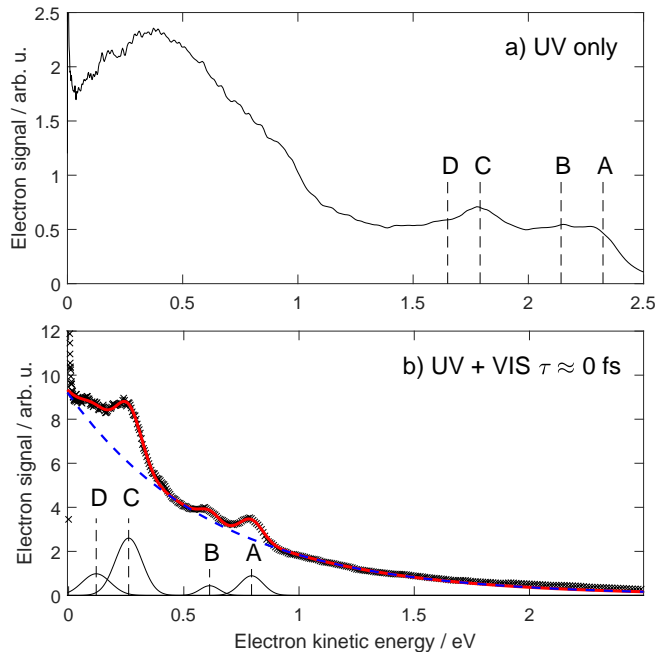


FIG. 1. a) One-color two-photon photoelectron spectrum of tetracene, recorded with a single fs laser pulse centered around 267 nm (4.64 eV). b) Two-color two-photon photoelectron spectrum recorded for temporally overlapping ($\tau \approx 0$ fs) laser pulses centered at 267 and 400 nm (4.64 and 3.1 eV). c) Two-color two-photon photoelectron spectrum recorded with an ionizing 400 nm laser pulse arriving $\tau \approx 200$ fs after the 267 nm excitation pulse. The blue full line in b) and c) shows a least squares fit to the experimental data (symbols) with a model consisting of Gaussian peaks (thin black lines) and an exponential background (thick red line).

shifted according to the lower ionizing photon energy. The photoelectron spectra in panel b) shows a prominent exponential background, which is caused by quasi-thermal electron emission previously observed for other PAH interacting with intense fs laser pulses[40, 54–56]. This autoionization process occurs after the absorption of several photons and creates a hot electronic subsystem that cannot equilibrate with the nuclear degrees of freedom on this ultrafast timescale. Close inspection of the photoelectron spectrum in figure 1 a) shows that the quasi-thermal electron emission is also present in the UV only spectrum, albeit significantly less pronounced. To extract reliable positions of the observed photoelectron features as well as delay dependent intensities in the presence of the pronounced exponential background, we have performed a least squares fit of the two-color spectra employing a model consisting of an exponential background and a number of Gaussian bands:

$$f_{PE} = A e^{-\frac{\epsilon}{k_B T}} + \sum_{n_{peaks}=5} a_n e^{-\frac{-(\epsilon-\epsilon_n)^2}{\sigma_n^2}} \quad (2)$$

Data points at electron kinetic energies below 0.03 eV and above 1.4 eV were excluded from the fit. Below 0.03 eV there is a signal of zero kinetic energy electrons and above 1.4 eV

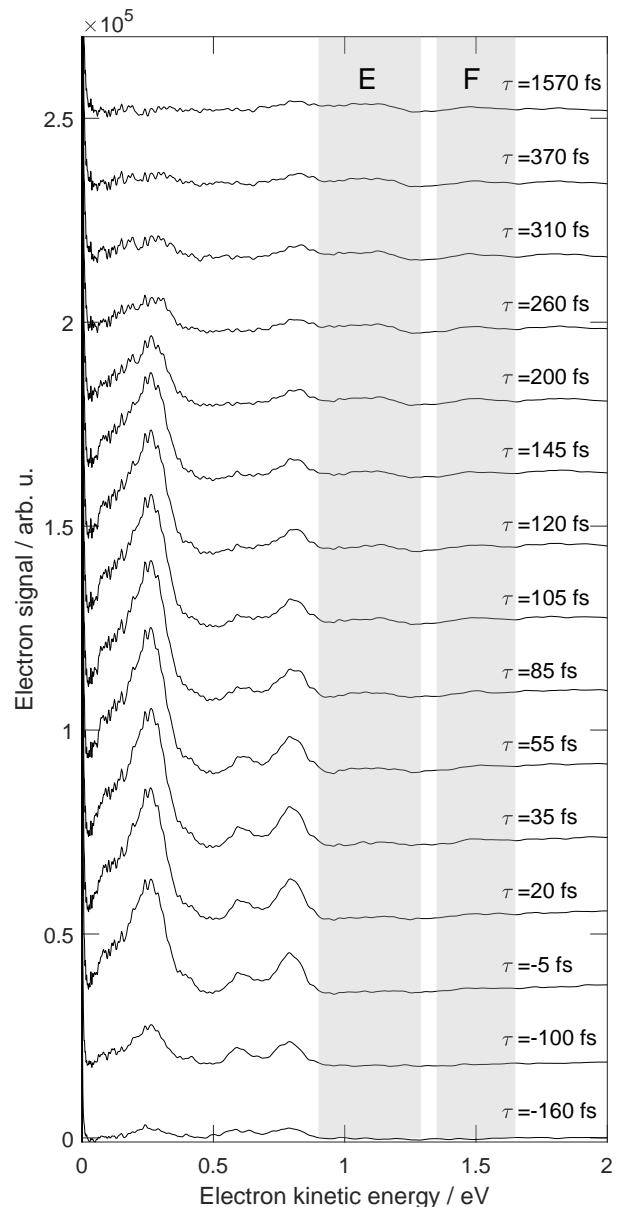


FIG. 2. Photoelectron spectra recorded for selected time delays between the UV and VIS pulses, after subtraction of exponential signal contributions obtained from the least-squares fit. Gray-shaded areas labeled E and F indicate the position of two weak features arising at positive delay times.

there are weak features in addition to the exponential background (see discussion below). To keep the fitting procedure stable and avoid overfitting, both of them are not included in the current fit model. The fit is performed in a global fashion, such that for all pump-probe delays only one global set of five Gaussian band positions and band widths is fitted, while the amplitudes of the Gaussians and of the exponential background are fitted for each delay individually. The resulting fit for zero time delay is included in figure 1 b) as

a solid red line with the exponential and Gaussian components shown separately as a blue dashed and a black solid line, respectively. Vertical dashed lines indicate the positions of the Gaussian bands. The fitting procedure retrieves band positions $E_{\text{PE}}^{\text{A/B/C/D}}$ of 0.79 eV, 0.61 eV, 0.26 eV and 0.12 eV for the photoelectron bands A-D. Feature A ($E_{\text{PE}}^{\text{A}}=0.79$ eV) is in agreement with a state of excitation energy 4.66 eV ($E_{\text{ex}}^{\text{A}} = \text{IP} + E_{\text{PE}} - v_{\text{probe}}$) in good agreement with the used UV photon energy. A possible explanation of the other bands is the population of several lower-lying neutral excited states of tetracene, occurring via non-adiabatic relaxation of the molecule within the duration of the fs laser pulses. While absorption studies did not report electronic states between the brightest state in the UV (≈ 4.82 eV[21]) and the lowest-lying bright state S_1 (2.77 eV)[18, 19, 21], different theoretical works[24, 28, 29, 35] predict a number of dark states in that region as well, supporting this explanation.

Figure 2 shows the two-color photoelectron spectra for different delays between the excitation (UV) and ionization (VIS) pulses. For better visibility of the individual bands the exponential signal component obtained from the fitting procedure has been removed and the spectra are separated by vertical offsets. The bands labeled A-D above show a pronounced time-dependence in agreement with the transient population and depopulation of lower-lying states by non-adiabatic dynamics. In addition to these bands, signals rising toward later delay times seem to appear in the two gray-shaded areas labeled E and F. Due to their weak intensities, we did not include these bands in the fit model. Neutral states lying higher in energy than the initially excited state (4.66 eV) cannot be populated over time. However, the features E and F located at $E_{\text{PE}}^{\text{E}}=1.1$ eV and $E_{\text{PE}}^{\text{F}}=1.5$ eV, respectively, can be explained by lower lying excited states ionized by two probe photons from the VIS pulse.

B. Comparison with calculations

The calculated vertical state energies of neutral tetracene and their respective oscillator strengths f to the ground state S_0 are shown in table I. Furthermore, table II provides the energies of the three lowest-lying doublet states of the radical cation, calculated at the equilibrium structure of the tetracene cation, and the Dyson intensities between the respective neutral and cationic states. For comparison, we also give the experimental values according to our assignments. These experimental values have been obtained from the fitted electron kinetic energy band position ($E_{\text{PE}}^{\text{A/C/D}}$) of features A, C, and D, the known ionization potential of ($\text{IP} = 6.97$ eV[49]) and the probe photon energy ($v_{\text{probe}} = 3.1$ eV) as $E_{\text{ex}}^{\text{A/C/D}} = \text{IP} + E_{\text{PE}} - v_{\text{probe}}$. For features E and F the corresponding expression takes into account the ionization energy to the two lowest-lying excited cationic states ($\text{IP}_2 = 8.41$ eV[49, 85]), and twice the probe photon energy to account for the two-photon ionization process, $E_{\text{ex}}^{\text{F}} = \text{IP}_2 + E_{\text{PE}} - 2v_{\text{probe}}$. Note, that assuming two-photon ionization to the cationic ground state would yield unphysical negative excitation energies for

TABLE I. Comparison of experimentally observed photoelectron band positions E_{PE} , excitation energies to which these states correspond E_{ex} and calculated excitation energies E_{theo} of the six lowest-lying singlet excited electronic states of tetracene.

| Left ^a state | experiment | | | theory | |
|----------------------------|------------|-----------------------------|-----------------------------|-----------------------------------|----------|
| | feature | $E_{\text{PE}} / \text{eV}$ | $E_{\text{ex}} / \text{eV}$ | $E_{\text{theo}} / \text{eV} (f)$ | symmetry |
| S_1 | | | 2.77 ^a | 2.75 (0.081) | B_{2u} |
| S_2 | E | 1.1 | 3.3 | 3.45 (0.002) | B_{3u} |
| S_3 | F | 1.5 | 3.7 | 3.83 (0.000) | A_g |
| S_4 | D | 0.12 | 3.99 | 4.04 (0.000) | B_{1g} |
| S_5 | C | 0.26 | 4.13 | 4.17 (0.000) | B_{1g} |
| S_6 | A/B | 0.79 | 4.66 | 4.83 (2.732) | B_{3u} |

^a a: value taken from Amirav *et al.* [19]

the features E and F. See also figure 3 for a sketch of the ionization scheme, and energy level diagram.

The largest oscillator strength was calculated for the S_6 state, which indicates that it is the high-lying bright state. Moreover, the energy of 4.83 eV calculated for the S_6 state agrees well with the maximum of the absorption spectrum observed for tetracene vapor (≈ 4.82 eV)[21]. Our experimental value of 4.64 eV, determined by the choice of our UV photon energy, is located in the rising flank of this strong absorption band, consisting of an unresolved broad vibrational progression. Thus, it seems clear that our UV excitation populates a set of vibrational states of the S_6 state, below its vertical excitation. This excitation gives rise to the feature A in the photoelectron spectrum upon ionization with the VIS probe pulse. The experimentally observed feature B would correspond to an excitation energy of 4.48 eV which is not in agreement with any of the calculated neutral excited states. Feature B is located 0.18 eV below feature A, and can thus be explained as an ionizing transition from the same initial state as feature A toward the first vibrationally excited state of the cationic ground state. The vibrational splitting observed in XUV photoelectron spectra of ground state tetracene was reported to be 0.17 eV [47, 49, 50], which is in good agreement with our observed splitting of 0.18 eV.

A similar splitting of 0.14 eV is also observed between the states deduced from features C and D. However, in this case the calculations also show two dark states S_5 and S_4 of B_{1g} symmetry (4.17 eV and 4.04 eV) in excellent agreement with the experimental values of 4.13 eV and 3.99 eV. The separation between the features C and D, which deviates slightly from the expected vibrational splitting, favors an assignment as two separate electronic states S_5 and S_4 . If the bands C and D are nevertheless caused by two ionizing transitions of the same intermediate state, this state could either be the S_5 or the S_4 state. The small difference in the calculated excitation energy does not allow an unambiguous assignment. The unresolved nature of the photoelectron spectra (figure 2) does not allow a final conclusion, and would even support the combination of both possible explanations. The features will be further discussed below in the analysis of the dynamical photoelectron yields. The excited states deduced from the bands E and F located at excitation energies of 3.3 eV and 3.7 eV

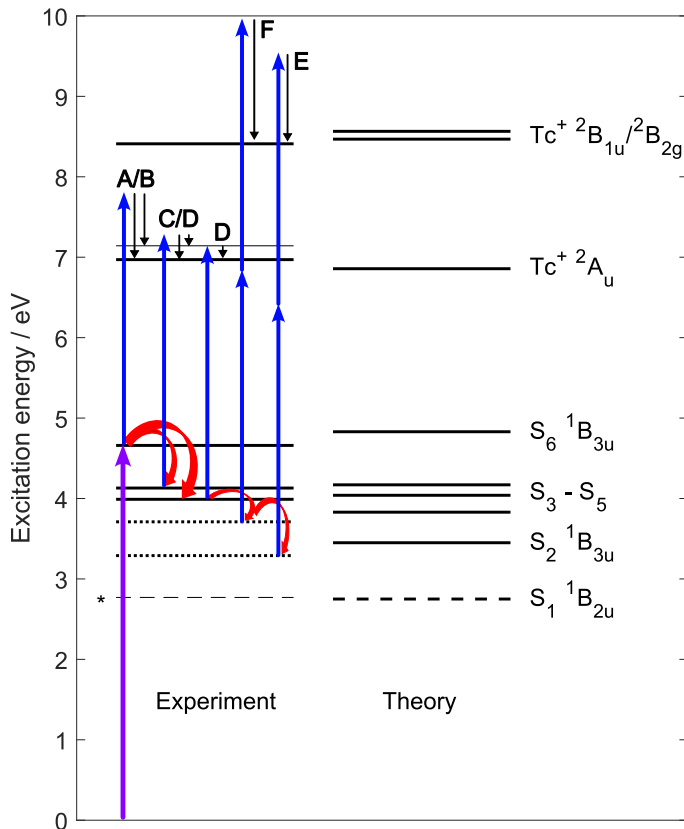


FIG. 3. Energy level diagram obtained from our photoelectron data and CASPT2 calculations. The additional line close to the $Tc^+ \ ^2A_u$ state indicates the first vibrationally excited state of the cation. Dotted lines indicate states deduced from weak features tentatively assigned to two-photon ionization to excited cationic states, while dashed lines indicate data for the S_1 state. Experimental excitation, relaxation and ionization pathways are indicated schematically. * Value taken from Ref. [18].

agree well with the calculated values for the S_2 (B_{3u} symmetry) and S_3 (A_g symmetry) states. To the best of our knowledge none of the states S_2 - S_5 have previously been observed and assigned experimentally. While the transitions from the ground state to the states S_3 - S_5 are forbidden by symmetry and expected to be dark, the transition to the S_2 state is expected to be weakly allowed, which agrees with its calculated oscillator strength. For the S_1 state the reported experimental value of 2.77 eV [18, 19] is in excellent agreement with our theoretical result of 2.75 eV. Furthermore, the vertical excitation energies of S_1 and S_2 agree very well with the reported energies in previous theoretical works [24, 28, 39]. The lowest-lying adiabatic ionization potentials of the radical cation agree well with the previously measured experimental values (further information about the vertical excitation energies is given in the supplementary material). The calculation of the Dyson intensities gives insight about likely transitions between the neutral and cationic states of the molecule [86]. The intensities of D_{S_1} , D_{S_2} , D_{S_4} and D_{S_6} to the cationic $Tc^+ \ ^2A_u$ state are much larger than D_{S_3} and D_{S_5} . The values of D_{S_4} , D_{S_5} and D_{S_6} as well as the probe photon energy of 3.1 eV

emphasize the one-photon ionization process from S_6 , S_5 and S_4 governing feature A/B and C/D, respectively. The Dyson intensities for the states S_2 and S_3 show that the ionization toward an excited cationic state is more likely than ionization to the cationic ground state. This supports our assignment of the features E and F as two-photon ionization signals of these states to the excited cationic states. The very low value of D_{S_3} for the cationic ground state $Tc^+ \ ^2A_u$ rationalizes that a corresponding two-photon ionization signal toward the cationic ground state cannot be observed in the photoelectron spectra. For the S_2 state the absence of such a photoelectron band (around 2.5 eV) is less clear from the values of D_{S_2} and has to be ascribed to the very low signal levels.

TABLE II. Comparison of the experimentally observed ionization potentials E_{IP} [49] to the calculated energies at the equilibrium structure of the radical cation E_{IP}^{theo} as well as the Dyson intensities D from different neutral states to the respective cationic state of tetracene.

| | $Tc^+ \ ^2A_u$ | $Tc^+ \ ^2B_{1u}$ | $Tc^+ \ ^2B_{2g}$ |
|----------------------|----------------|-------------------|-------------------|
| E_{IP} / eV | 6.97 | 8.41 | 8.41 |
| E_{IP}^{theo} / eV | 6.857 | 8.468 | 8.565 |
| D_{S_1} | 0.427 | 0.014 | 0.341 |
| D_{S_2} | 0.200 | 0.212 | 0.005 |
| D_{S_3} | 0.008 | 0.013 | 0.519 |
| D_{S_4} | 0.240 | 0.007 | 0.026 |
| D_{S_5} | 0.088 | 0.001 | 0.061 |
| D_{S_6} | 0.230 | 0.221 | 0.004 |

C. Relaxation dynamics

The fitting procedure described above was used to retrieve individual time-dependent photoelectron yields for four different Gaussian bands (A-D) observed in the two-color photoelectron spectra. For the two weaker contributions (E and F) an unambiguous retrieval of amplitudes was not possible, and we therefore refrain from discussing the details of the dynamics of these states further. The resulting photoelectron intensities are displayed as a function of the delay between pump and probe pulses in figure 4.

The yield of band A is maximal close to a nominal pump-probe delay of zero, and shows an approximate Gaussian shape with a plateau for positive pump-probe delays $\tau > 200$ fs. The almost Gaussian appearance is an indication that the shape is dominated by the experimental cross-correlation of the laser pulses, expected to be about 200 fs (FWHM). The yield of band B shows a similar Gaussian shape but its maximum seems slightly shifted to negative pump-probe delays and there is no plateau at positive pump-probe delays. The overall data quality for band B is lower, as shown by the errorbars ($\pm\sigma$, estimated from the covariance matrix of the model fit), due to the lower signal levels of this band.

Band C and D show maximal photoelectron yield at slightly positive pump-probe delays. Also both time-dependent photoelectron yields deviate from a Gaussian shape by a slight asymmetry toward positive delay times, in agreement with a

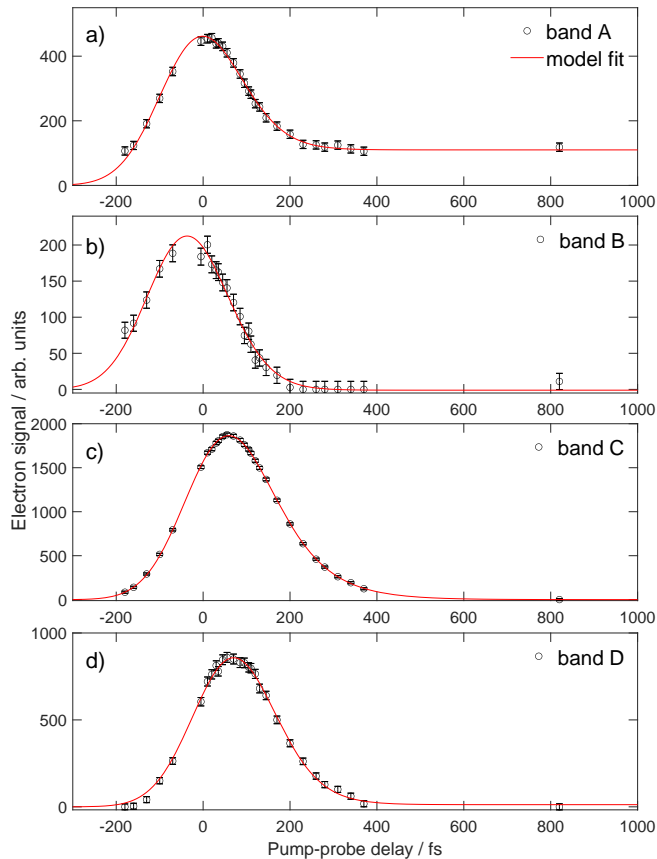


FIG. 4. Time-dependent photoelectron yields of the features A-D. The red solid lines are model fits obtained using a step function with an exponential decay, broadened by the experimental cross-correlation between the two laser pulses, see equation 3.

lifetime comparable to or longer than the cross-correlation of the laser pulses. The curve of the transient photoelectron yield of band D appears slightly more narrow than the one for band C, which indicates a shorter lifetime. To assess the observed differences more quantitatively, we fit all four transient photoelectron yields with a fit model according to

$$f(t) = Y_1 \cdot e^{-\frac{t-t_0}{\tau}} \cdot \left(1 + \operatorname{erf} \left(\frac{t-t_0}{\sqrt{2}\tau_{cc}} - \frac{\tau_{cc}}{\sqrt{2}\tau} \right) \right) + Y_2 \cdot \left(1 + \operatorname{erf} \left(\frac{t-t_0}{\sqrt{2}\tau_{cc}} \right) \right). \quad (3)$$

Y_i describe amplitudes, τ is the decay time of a state and τ_{cc} is the cross-correlation time. An effective zero time t_0 is explicitly included to account for and quantify the apparent shifts of the individual signals along the delay time axis. The second errorfunction term is included to account for possible plateaus, see figure 4 a). The cross-correlation time τ_{cc} was fixed in the fitting procedure for better comparability of the individual bands. The fixed value of 87 fs, corresponds to the value obtained for band C in an unconstrained fit. Only for band D the free fit produced a τ_{cc} significantly deviating from this value by about 10 fs. The results of the fitting procedure for

TABLE III. Obtained fit parameters for the transient photoelectron yields fitted individually. The cross-correlation was fixed at 87 fs ($\text{FWHM} = 2\sqrt{2\ln 2}\tau_{cc} = 204$ fs), the value determined in a free fit of band C. Errors given are 2σ estimated from the covariance matrix of the model fit.

| band | τ / fs | τ_{cc} / fs | t_0 |
|------|-------------|------------------|--------------|
| A | 44 ± 8 | 87 | -46 ± 6 |
| B | 38 ± 16 | 87 | -67 ± 12 |
| C | 85 ± 3 | 87 | -1 ± 3 |
| D | 48 ± 12 | 87 | 30 ± 4 |

the bands A-D are summarized in table III. The fitted parameters quantitatively describe what could already be observed in figure 4. Within errorbars, band A and B have the same decay times τ , significantly below τ_{cc} . Both have negative values of t_0 on the nominal time axis, with a more negative value for band B. Considering the uncertainties of the values this difference is however barely significant. Band C has a t_0 of zero and a decay time $\tau = 85$ fs, very similar to the cross-correlation time τ_{cc} , and band D is with $t_0 = 30$ fs even further shifted to positive delay times and has a decay time comparable to those of band A and B.

Bands A and B have above been assigned to the same initially excited electronic state, differing only by the vibrational excitation of the cationic ground state produced upon ionization. As such, we would expect the corresponding photoelectron yields to show an identical time-dependence. There is, however, a slight difference in the observed t_0 as well as the presence of a plateau in the yield of band A at large delay times, which is not present for band B. The plateau observed for band A at large delays can arise for example from a part of the population becoming trapped in the state. However, in this case we would expect the band B to be present as well, unless the trapped part of the population would assume a nuclear geometry very close to the cationic equilibrium structure. In this case the Franck-Condon factors, governing the relative intensity of band B could become very small. Figure 5 shows the signal of band B relative to the signal of band A, decreasing approximately linearly with the delay time. This behavior is in principle in agreement with a nuclear relaxation process of the tetracene molecule in its initially excited state toward the cationic equilibrium geometry.

Alternatively, the plateau in the yield of A may be explained by the internal conversion of a part of the initial population to a Rydberg state, that has been computed to lie in the same energy range[40]. This Rydberg state could lie very close in energy, while being closer to the cation in nuclear geometry. The geometry close to the cationic structure would avoid significant Franck-Condon factors for the ionization to the vibrationally excited cationic state, and thus explain the persistence of band A in the absence of band B at long delays.

The differences between the yields of bands C and D are, according to the fitted results, more significant than the differences between bands A and B. These differences include the shorter decay time τ as well as a more positive t_0 of band D. The occurrence of significant differences between the two

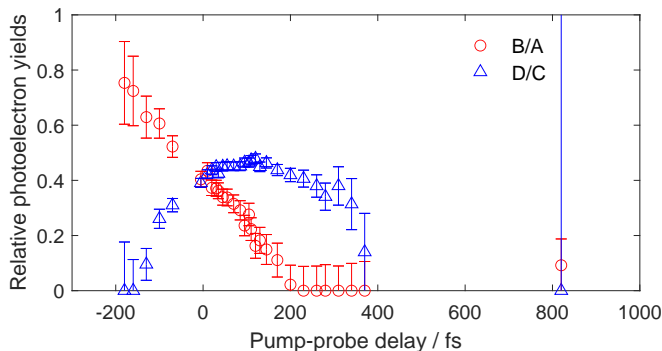


FIG. 5. Time-dependent relative photoelectron yields of bands B/A and D/C.

bands again suggests two different electronic states instead of vibrational structure in the photoionization of a single electronic state as the reason for the two photoelectron bands. The differences observed in the dynamics of the two bands is also reflected in the relative Franck-Condon factors depicted in figure 5. The ratio of the yields of bands C and D shows a complex behavior, not easily explained by the motion of a nuclear wavepacket on a potential energy surface. In combination with the band positions, we thus conclude that an assignment as two individual electronic states S_4 and S_5 seems more plausible than the interpretation as two ionizing transitions from the same electronic state. Nevertheless, it is not possible to fully rule out the latter explanation or a combination of the two.

In summary, our data is in agreement with an initial excitation of the high-lying bright state S_6 , which subsequently decays non-adiabatically via three dark states S_5 , S_4 and S_3 , into the state S_2 . Most likely, the tetracene molecules decay in a final non-radiative step into the lowest excited state S_1 before decaying by fluorescence back to the ground state. While we can deduce a lifetime of about 45 fs of the S_6 state, our current fitting procedure treating each state individually, cannot give fully quantitative results. This task would require a detailed global fitting procedure based on rate equations taking into account all possible channels between the observed states. Currently, in part also limited by the estimated cross-correlation of our laser pulses of 87 fs (200 fs FWHM), we cannot fully elucidate if the observed states are all populated consecutively or if there exist parallel decay channels. Nevertheless, the differences in the t_0 values obtained from bands A, C and D agree with the states S_5 and S_4 being populated on slightly different timescales.

The non-adiabatic dynamics following the excitation to the brightest singlet state of tetracene and other PAH have previously been calculated by Posenitskiy *et al.* [61, 62] based on a surface hopping algorithm using time-dependent density functional tight binding surfaces. In these works an initial population of the brightest excited state is predicted to decay within 65 fs [62] toward a set of lower lying excited states. At the end of the 300 fs simulation window, there remains 8% of the initial population in the initially excited brightest state. The

results from these theoretical studies agree qualitatively with our experimental observations, including the fast timescale of the depopulation of the initially excited state and the transient population of intermediate states. A detailed comparison seems however infeasible, since the number of states predicted between the initially excited state and the ground state differs.

IV. CONCLUSION

We have studied the ultra-fast dynamics of gas phase tetracene excited in the UV range with time-resolved photoelectron spectroscopy. Despite various background signals and many competing processes that occur in the interaction of PAH with femtosecond laser pulses, we could extract the signatures of the valence states that are transiently populated in the relaxation process. Using high-level *ab-initio* calculations, we have characterized the low-lying singlet excited states of neutral tetracene and low-lying ionization potentials, calculated at the equilibrium structure of its radical cation. Comparing the experimental results and the calculations, we were able to assign the involved intermediate states to a series of dark states S_3 - S_5 of B_{1g} and A_g symmetry and to the S_2 state of B_{3u} symmetry. None of these states have to the best of our knowledge previously been measured or assigned experimentally, highlighting the power of time-resolved photoelectron spectroscopy in tracking excited state dynamics without restrictions due to dark states. The initial population in the S_6 state decays within ≈ 45 fs. If the lower-lying states are all populated consecutively or partially in parallel, cannot be conclusively decided from our data, due to limitations of the achievable time-resolution. More reliable detection of the two low-lying states S_2 and S_3 could be achieved with higher probe photon energies, allowing single-photon ionization of these states. The future extension of these studies to higher probe energies supported by high-level quantum chemical calculations on polyacenes will provide deeper insights into the relaxation dynamics of this class of molecules.

CONFLICTS OF INTEREST

There are no conflicts to declare.

ACKNOWLEDGEMENTS

We gratefully acknowledge funding from the Deutsche Forschungsgemeinschaft (grant numbers STI 125/25-1, RTG 2717) and the COST Action CA21101 “Confined Molecular Systems: From a New Generation of Materials to the Stars (COSY)”. Furthermore, the authors acknowledge support by the state of Baden-Württemberg through bwHPC and the German Research Foundation (DFG) through grant no INST 40/575-1 FUGG (JUSTUS 2 cluster). The authors gratefully acknowledge the funding of this project by computing time provided by the Paderborn Center for Parallel Computing (PC2). We thank Prof. Henrik Stapelfeldt

for sharing and discussing his unpublished results with us. A. S. acknowledges fruitful discussions with and support provided by Evgeny Posenitskyi, Mathias Rapacioli, Frank Lépine and Bernd v. Issendorff. P.B.C. acknowledges financial support under grant PID2021-124080OB-I00 funded by MCIN/AEI/10.13039/501100011033 and ERDF A way of

Making Europe.

DATA AVAILABILITY STATEMENT

All data not provided in the supplementary material are available from the corresponding author upon reasonable request.

-
- [1] J. Anthony, *Angew. Chem. Int. Ed.* **47**, 452 (2008).
- [2] T. M. Clarke and J. R. Durrant, *Chem. Rev.* **110**, 6736 (2010).
- [3] J. D. Myers and J. Xue, *Polym. Rev.* **52**, 1 (2012).
- [4] A. G. G. M. Tielens, *EAS Pub. Ser.* **46**, 3 (2011).
- [5] C. Joblin and A. G. G. M. Tielens, *EDP Sciences* (2020), 10.1051/978-2-7598-2482-3.
- [6] A. Omont, *A&A* **590**, A52 (2016).
- [7] J. Li, M. Wang, S. Ren, X. Gao, W. Hong, H. Li, and D. Zhu, *J. Mater. Chem.* **22**, 10496 (2012).
- [8] J. A. Rogers, Z. Bao, K. Baldwin, A. Dodabalapur, B. Crone, V. R. Raju, V. Kuck, H. Katz, K. Amundson, J. Ewing, and P. Drzaic, *Proc. Natl. Acad. Sci. U.S.A.* **98**, 4835 (2001).
- [9] J. Xia, S. N. Sanders, W. Cheng, J. Z. Low, J. Liu, L. M. Campos, and T. Sun, *Adv. Mater.* **29**, 1601652 (2017).
- [10] S. Izadnia, D. W. Schönleber, A. Eisfeld, A. Ruf, A. C. LaForge, and F. Stienkemeier, *J. Phys. Chem. Lett.* **8**, 2068 (2017).
- [11] J. Hoche, M. Flock, X. Miao, L. N. Philipp, M. Wenzel, I. Fischer, and R. Mitric, *Chem. Sci.* **12**, 11965 (2021).
- [12] M. Bohlen, R. Michiels, M. Michelbach, S. Ferchane, M. Walter, A. Eisfeld, and F. Stienkemeier, *J. Chem. Phys.* **156**, 034305 (2022).
- [13] A. S. Bogomolov, V. M. Rogoveshko, and A. V. Baklanov, *AIP Adv.* **13**, 015102 (2023).
- [14] L. Colangeli, V. Mennella, G. A. Baratta, E. Bussolati, and G. Strazzula, *Astrophys. J.* **396**, 369 (1992).
- [15] J. Oomens, A. G. G. M. Tielens, B. G. Sartakov, G. von Helden, and G. Meijer, *Astrophys. J.* **591**, 968 (2003).
- [16] A. K. Lemmens, D. B. Rap, J. Thunnissen, S. Gruet, A. L. Steber, S. Panchagnula, A. G. G. M. Tielens, M. Schnell, W. J. Buma, and A. M. Rijs, *J. Phys. Chem. Lett.* **11**, 8997 (2020).
- [17] A. Marciniak, V. Despré, T. Barillot, A. Rouzée, M. C. E. Galbraith, J. Klei, C. H. Yang, C. T. L. Smeenk, V. Lorient, S. N. Reddy, A. G. G. M. Tielens, S. Mahapatra, A. I. Kuleff, M. J. J. Vrakking, and F. Lépine, *Nat. Commun.* **6**, 7909 (2015).
- [18] A. Amirav, U. Even, and J. Jortner, *J. Chem. Phys.* **71**, 2319 (1979).
- [19] A. Amirav, U. Even, and J. Jortner, *J. Chem. Phys.* **75**, 3770 (1981).
- [20] T. Jiro, *Bull. Chem. Soc. Jpn.* **38**, 86 (1965).
- [21] G. C. Morris, *J. Mol. Spectrosc.* **18**, 42 (1965).
- [22] S. Canuto, M. C. Zerner, and G. H. F. Dierksen, *Astrophys. J.* **377**, 150 (1991).
- [23] H. H. Heinze, A. Görling, and N. Rösch, *J. Chem. Phys.* **113**, 2088 (2000).
- [24] S. Grimme and M. Parac, *ChemPhysChem* **4**, 292 (2003).
- [25] J. J. Dorando, J. Hachmann, and G. K.-L. Chan, *J. Chem. Phys.* **127**, 084109 (2007).
- [26] J. Hachmann, J. J. Dorando, M. Avilés, and G. K.-L. Chan, *J. Chem. Phys.* **127**, 134309 (2007).
- [27] P. Sony and A. Shukla, *Phys. Rev. B* **75**, 155208 (2007).
- [28] C. M. Marian and N. Gilka, *J. Chem. Theory Comput.* **4**, 1501 (2008).
- [29] S. Knippenberg, J. H. Starcke, M. Wormit, and A. Dreuw, *Mol. Phys.* **108**, 2801 (2010).
- [30] K. Lopata, R. Reslan, M. Kowalska, D. Neuhauser, N. Govind, and K. Kowalski, *J. Chem. Theory Comput.* **7**, 3686 (2011).
- [31] K. Pelzer, L. Greenman, G. Gidofalvi, and D. A. Mazziotti, *J. Phys. Chem. A* **115**, 5632 (2011).
- [32] V. Sauri, L. Serrano-Andrés, A. R. M. Shahi, L. Gagliardi, S. Vancoillie, and K. Pierloot, *J. Chem. Theory Comput.* **7**, 153 (2011).
- [33] P. M. Zimmerman, F. Bell, D. Casanova, and M. Head-Gordon, *J. Am. Chem. Soc.* **133**, 19944 (2011).
- [34] D. Casanova, *J. Chem. Theory Comput.* **10**, 324 (2014).
- [35] Y. Kurashige and T. Yanai, *Bull. Chem. Soc. Jpn.* **87**, 1071 (2014).
- [36] T. Yanai, Y. Kurashige, W. Mizukami, J. Chalupský, T. N. Lan, and M. Saitow, *Int. J. Quantum Chem.* **115**, 283 (2015).
- [37] D. Casanova and A. I. Krylov, *J. Chem. Phys.* **144**, 014102 (2016).
- [38] Y. Yang, E. R. Davidson, and W. Yang, *Proc. Natl. Acad. Sci. U.S.A.* **113**, E5098 (2016).
- [39] F. Bettanin, L. F. A. Ferrão, M. Pinheiro, A. J. A. Aquino, H. Lischka, F. B. C. Machado, and D. Nachtigallova, *J. Chem. Theory Comput.* **13**, 4297 (2017).
- [40] E. Bohl, B. Mignolet, J. O. Johansson, F. Remacle, and E. E. B. Campbell, *Phys. Chem. Chem. Phys.* **19**, 24090 (2017).
- [41] F. Plasser, S. A. Mewes, A. Dreuw, and L. González, *J. Chem. Theory Comput.* **13**, 5343 (2017).
- [42] D. C. A. Valente, M. T. do Casal, M. Barbatti, T. A. Niehaus, A. J. A. Aquino, H. Lischka, and T. M. Cardozo, *J. Chem. Phys.* **154**, 044306 (2021).
- [43] A. Manian and S. P. Russo, *Sci. Rep.* **12**, 21481 (2022).
- [44] A. Pomogaeva, M. Filatov, and C. H. Choi, *Carbon Trends* **7**, 100146 (2022).
- [45] Y. Dai, J.-C. Sancho-García, and F. Negri, *Chemistry* **5**, 616 (2023).
- [46] A. Dreuw and P. Tegeder, *Phys. Chem. Chem. Phys.* **25**, 17079 (2023).
- [47] P. A. Clark, F. Brogli, and E. Heilbronner, *Helv. Chim. Acta* **55**, 1415 (1972).
- [48] F. Brogli and E. Heilbronner, *Angew. Chem.* **84**, 551 (1972).
- [49] W. Schmidt, *J. Chem. Phys.* **66**, 828 (1977).
- [50] V. Coropceanu, M. Malagoli, D. A. da Silva Filho, N. E. Gruhn, T. G. Bill, and J. L. Brédas, *Phys. Rev. Lett.* **89**, 275503 (2002).
- [51] J. A. Noble, C. Aupetit, D. Descamps, S. Petit, A. Simon, J. Mascetti, N. Ben Amor, and V. Blanchet, *Phys. Chem. Chem. Phys.* **21**, 14111 (2019).
- [52] W. Radloff, V. Stert, T. Freudenberg, I. V. Hertel, C. Jouvet, C. Dedonder-Lardeux, and D. Solgadi, *Chem. Phys. Lett.* **281**, 20 (1997).

- [53] V. Blanchet, K. Raffael, G. Turri, B. Chatel, B. Girard, I. A. Garcia, I. Wilkinson, and B. J. Whitaker, *J. Chem. Phys.* **128**, 164318 (2008).
- [54] M. Kjellberg, A. V. Bulgakov, M. Goto, O. Johansson, and K. Hansen, *J. Chem. Phys.* **133**, 074308 (2010).
- [55] J. O. Johansson and E. E. B. Campbell, *Chem. Soc. Rev.* **42**, 5661 (2013).
- [56] J. O. Johansson, G. G. Henderson, and E. E. B. Campbell, *J. Phys. Chem. A* **118**, 8067 (2014).
- [57] N. Kuthirummal and P. M. Weber, *Chem. Phys. Lett.* **378**, 647 (2003).
- [58] C. P. Schick and P. M. Weber, *J. Phys. Chem. A* **105**, 3725 (2001).
- [59] R. Spesyvtsev, O. M. Kirkby, M. Vacher, and H. H. Fielding, *Phys. Chem. Chem. Phys.* **14**, 9942 (2012).
- [60] H. Reisler and K. A. I., *Int. Rev. Phys. Chem.* **28**, 267 (2009).
- [61] E. Posenitskiy, M. Rapacioli, B. Lepetit, D. Lemoine, and F. Spiegelman, *Phys. Chem. Chem. Phys.* **21**, 12139 (2019).
- [62] E. Posenitskiy, M. Rapacioli, D. Lemoine, and F. Spiegelman, *J. Chem. Phys.* **152**, 074306 (2020).
- [63] N. Rendler, A. Scognamiglio, M. Barranco, M. Pí, N. Halberstadt, K. Dulitz, and F. Stienkemeier, *J. Phys. Chem. A* **125**, 9048 (2021).
- [64] B. Dick, *Phys. Chem. Chem. Phys.* **16**, 570 (2014).
- [65] S. H. Vosko, L. Wilk, and M. Nusair, *Can. J. Phys.* **58**, 1200 (1980).
- [66] A. D. Becke, *Phys. Rev. A* **38**, 3098 (1988).
- [67] C. Lee, W. Yang, and R. G. Parr, *Phys. Rev. B* **37**, 785 (1988).
- [68] A. D. Becke, *J. Chem. Phys.* **96**, 2155 (1992).
- [69] A. D. Becke, *J. Chem. Phys.* **98**, 5648 (1993).
- [70] F. Weigend and R. Ahlrichs, *Phys. Chem. Chem. Phys.* **7**, 3297 (2005).
- [71] S. Grimme, J. Antony, S. Ehrlich, and H. Krieg, *J. Chem. Phys.* **132**, 154104 (2010).
- [72] S. Grimme, S. Ehrlich, and L. Goerigk, *J. Comput. Chem.* **32**, 1456 (2011).
- [73] "TURBOMOLE V7.5 2020, a development of University of Karlsruhe and Forschungszentrum Karlsruhe GmbH, 1989-2007, TURBOMOLE GmbH, since 2007; available from <http://www.turbomole.com>."
- [74] K. Andersson and B. O. Roos, *Int. J. Quantum Chem.* **45**, 591 (1993).
- [75] T. Helgaker, P. Jørgensen, and J. Olsen, *Molecular Electronic-Structure Theory* (John Wiley & Sons, Ltd, 2000).
- [76] P.-O. Widmark, P.-Å. Malmqvist, and B. O. Roos, *Theoret. Chim. Acta* **77**, 291 (1990).
- [77] P.-O. Widmark, B. J. Persson, and B. O. Roos, *Theoret. Chim. Acta* **79**, 419 (1991).
- [78] R. Pou-Amérgigo, M. Merchán, I. Nebot-Gil, P.-O. Widmark, and B. O. Roos, *Theoret. Chim. Acta* **92**, 149 (1995).
- [79] K. Pierloot, B. Dumez, P.-O. Widmark, and B. O. Roos, *Theoret. Chim. Acta* **90**, 87 (1995).
- [80] N. Forsberg and P.-Å. Malmqvist, *Chem. Phys. Lett.* **274**, 196 (1997).
- [81] G. Ghigo, B. O. Roos, and P.-Å. Malmqvist, *Chem. Phys. Lett.* **396**, 142 (2004).
- [82] B. N. C. Tenorio, A. Ponzí, S. Coriani, and P. Decleva, *Molecules* **27**, 1203 (2022).
- [83] F. Aquilante, J. Autschbach, R. K. Carlson, L. F. Chibotaru, M. G. Delcey, L. De Vico, I. Fdez. Galván, N. Ferré, L. M. Frutos, L. Gagliardi, M. Garavelli, A. Giussani, C. E. Hoyer, G. Li Manni, H. Lischka, D. Ma, P.-Å. Malmqvist, T. Müller, A. Nenov, M. Olivucci, T. B. Pedersen, D. Peng, F. Plasser, B. Pritchard, M. Reiher, I. Rivalta, I. Schapiro, J. Segarra-Martí, M. Stenrup, D. G. Truhlar, L. Ungur, A. Valentini, S. Vancoillie, V. Veryazov, V. P. Vysotskiy, O. Weingart, F. Zapata, and R. Lindh, *J. Comput. Chem.* **37**, 506 (2016).
- [84] I. Fdez. Galván, M. Vacher, A. Alavi, C. Angeli, F. Aquilante, J. Autschbach, J. J. Bao, S. I. Bokarev, N. A. Bogdanov, R. K. Carlson, L. F. Chibotaru, J. Creutzberg, N. Dattani, M. G. Delcey, S. S. Dong, A. Dreuw, L. Freitag, L. M. Frutos, L. Gagliardi, F. Gendron, A. Giussani, L. González, G. Grell, M. Guo, C. E. Hoyer, M. Johansson, S. Keller, S. Knecht, G. Kovačević, E. Källman, G. Li Manni, M. Lundberg, Y. Ma, S. Mai, J. P. Malhado, P.-Å. Malmqvist, P. Marquetand, S. A. Mewes, J. Norell, M. Olivucci, M. Oppel, Q. M. Phung, K. Pierloot, F. Plasser, M. Reiher, A. M. Sand, I. Schapiro, P. Sharma, C. J. Stein, L. K. Sørensen, D. G. Truhlar, M. Ugandi, L. Ungur, A. Valentini, S. Vancoillie, V. Veryazov, O. Weser, T. A. Wesolowski, P.-O. Widmark, S. Wouters, A. Zech, J. P. Zobel, and R. Lindh, *J. Chem. Theory Comput.* **15**, 5925 (2019).
- [85] J. Szczepanski, J. Drawdy, C. Wehlburg, and M. Vala, *Chem. Phys. Lett.* **245**, 539 (1995).
- [86] W. Arbelo-González, R. Crespo-Otero, and M. Barbatti, *J. Chem. Theory Comput.* **12**, 5037 (2016).

Supplementary Material for: Non-adiabatic electronic relaxation of tetracene from its brightest singlet state

Audrey Scognamiglio,^{a‡} Karin S. Thalmann,^{a‡} Sebastian Hartweg,^{*a‡}
Nicolas Rendler^a, Lukas Bruder,^a Pedro B. Coto,^b Michael Thoss,^a
Frank Stienkemeier^a

* e-mail: sebastian.hartweg@physik.uni-freiburg.de

^a University of Freiburg, Institute of Physics, Hermann-Herder-Str. 3, Freiburg, Germany

^b Materials Physics Center (CFM), CSIC and Donostia International Physics Center (DIPC),
Paseo Manuel de Lardizabal 5, 20018 Donostia - San Sebastián, Spain

S1 Details on background subtraction

Figure S1 shows the two-color photoelectron spectra obtained by the UV and VIS pulses prior to background subtraction (black solid lines) at a delay of $\tau \approx 0$ fs a) and $\tau = -1430, -680$ and -430 fs b). The latter curves overlap almost perfectly, and are thus not visible as individual curves. The single-color backgrounds obtained with only the VIS (red lines) and only the UV pulses (blue lines) are shown in both panels, together with the background subtracted spectra (cyan lines). The background subtracted spectra at negative delays show an exponentially decaying feature, with a single edge-like band on top, located at ≈ 0.43 eV. This feature agrees well with the S_1 state (excitation energy 2.77 eV²), ionized by the UV laser pulse. Note that the VIS pulse with a photon energy of 3.1 eV is in resonance with a vibrationally excited S_1 state, thus explaining the possible population of the S_1 state at negative pump-probe delays (i.e. the VIS pulse arriving prior to the UV pulse).

To remove the pump-probe effect of exciting the tetracene molecules with the VIS pulse and probing with the UV pulse, we averaged the spectra obtained at the three negative delays given above (i.e. the three overlapping cyan lines in figure S1 b)). Given the fact that the S_1 state in the tetracene molecule has a lifetime of several nanoseconds[?], we can deduce the time-dependence of this pump-probe signal. The S_1 state should show a relative population increasing in a step-like fashion, broadened by the cross correlation of the laser pulses, given by

$$p_{S_1}(t) = \frac{1}{2} \cdot \left(1 + \operatorname{erf} \left(-\frac{t}{\sqrt{2}\tau_{cc}} \right) \right), \quad (1)$$

where t is the time delay between the UV and VIS pulses and τ_{cc} is the cross correlation width. We multiply the averaged signal described above with the corresponding population according to equation 1 and subtract it from the time-resolved photoelectron spectra at the corresponding delay time. The effect of this additional background subtraction is depicted in figure S1, where panel a) depicts data without the subtraction of the VIS pump- UV probe signal, and the data including this subtraction is shown in panel b).

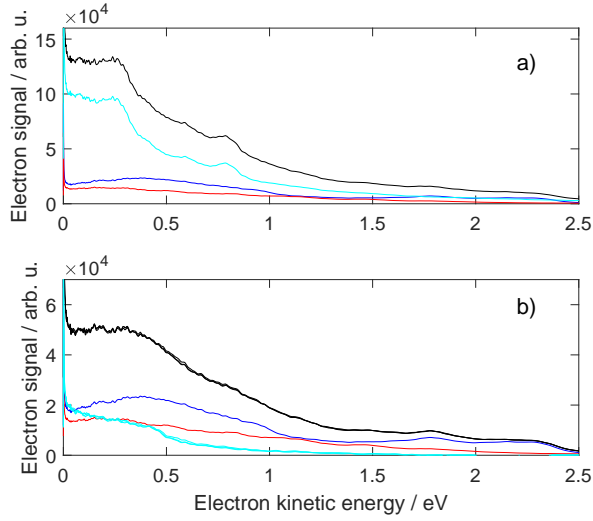


Figure S1: Single-color background subtraction from time-resolved two-color photoelectron spectra at a) $\tau \approx 0$ fs and b) $\tau = -1430, -680$ and -430 fs (lines overlapping). Black solid lines show data prior to background subtraction, blue shows the UV only background, red the VIS only background and cyan lines show data after background subtraction.

S2 Details on least squares fit of the spectra

The obtained fits for the spectra are displayed in figure S1 b). The time-dependent amplitude and decay constant of the exponential signal component are displayed in figure S2, while the time-dependent amplitudes of the Gaussian signals are shown in the main text. The obtained Gaussian band positions are 0.120, 0.261, 0.0612, 0.794, and 1.047 eV, with widths (σ) of 0.061, 0.058, 0.041, 0.050, and 0.115 eV.

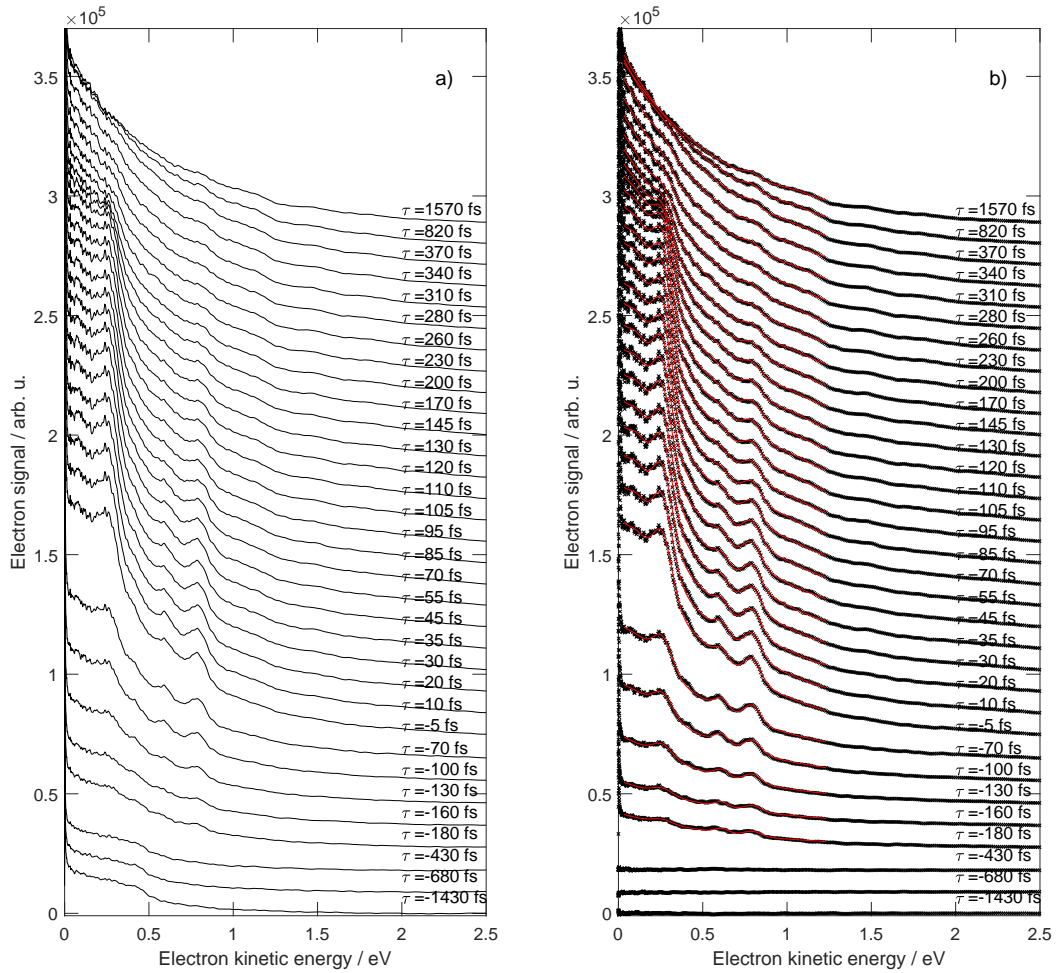


Figure S2: Time-resolved photoelectron spectra without (panel a)) and with (panel b)) subtraction of the VIS pump-UV probe signals. Delays between the laser pulses are indicated for every spectrum. In panel b) we additionally include the results obtained from the least squares fit.

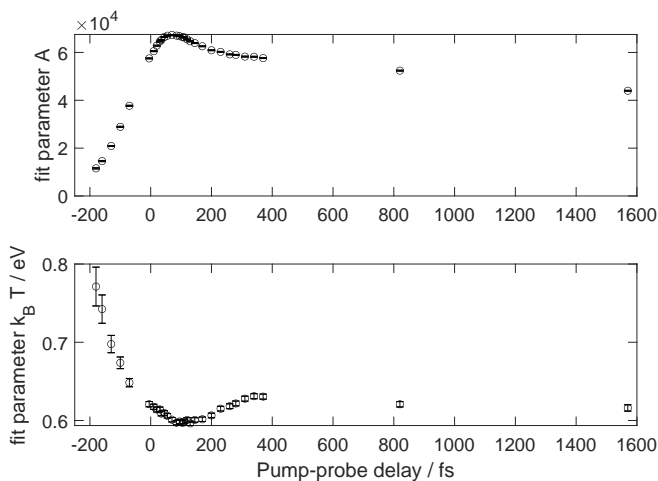


Figure S3: Obtained fit parameters for the exponential signal components of the photoelectron spectra at different pump-probe delays. Top panel: Exponential amplitude. Bottom panel: Decay constant.

S3 Computational details

In this section, additional information on the computational results for the excitation energies of tetracene in its neutral and cation ground state equilibrium structure is provided and the calibration of the calculations is discussed.

S3.1 Details on the electronic structure calculation of neutral tetracene

As described in the main paper, the electronic structure of the neutral tetracene was calculated using a 15 state-averaged CASSCF/CASPT2[?] calculation with an active space of 16 active electrons and 16 active orbitals. The calculations were carried out using MOLCAS 8.4[?] and OpenMOLCAS v20.10[?]. The optimized orbitals of the active space of this calculation are shown in table S4.

S3.2 Ionization potentials and Dyson intensities

For a complete picture of tetracene as a radical cation, the vertical excitation energies from the ground state equilibrium structure of the neutral tetracene to its cationic states are provided in table S1. The calculations were performed using a 15 state-averaged CASSCF/CASPT2 calculation with an active space of 16 active electrons and 16 active orbitals (similar to the calculation of neutral tetracene). In addition, the Dyson intensities[?] were calculated for transitions from the different neutral states to the respective cationic state. The calculation described above was carried out using MOLCAS 8.4[?] and OpenMOLCAS v20.10[?]. The results are shown in table S1.

The vertical ionization potentials as shown in table S1 for $\text{Tc}^+ \ ^2\text{A}_u$ and $\text{Tc}^+ \ ^2\text{B}_{1u}$ agree well with the experimental values and are comparable with the ionization potentials in table 2. The ionization potential of $\text{Tc}^+ \ ^2\text{B}_{2g}$ is significantly larger than the experimental value and not accurately described. Thus, the relaxation of the cation to its ground state equilibrium structure is crucial for a reasonable description of the cationic states. The trends of the Dyson intensities in table 2, however, can also be observed in table S1 and the values do not differ significantly. This emphasizes the accuracy of the calculated Dyson intensities.

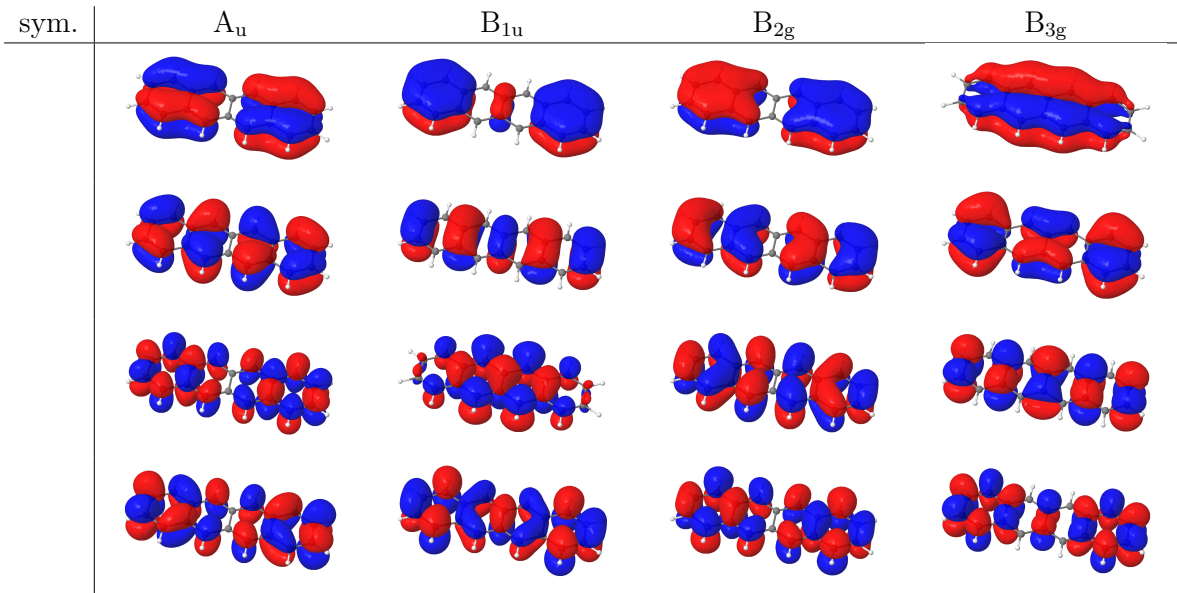


Figure S4: CASSCF optimized state-average orbitals and their corresponding symmetry (irreducible representation of point group D_{2h}). In the state-averaged calculations, 15 roots with 16 active orbitals and 16 active electrons were employed.

| | $Tc^+ \ ^2A_u$ | $Tc^+ \ ^2B_{1u}$ | $Tc^+ \ ^2B_{2g}$ |
|------------------------------------|----------------|-------------------|-------------------|
| E_{IP} / eV | 6.97 | 8.41 | 8.41 |
| $E_{IP}^{\text{theo}} / \text{eV}$ | 6.938 | 8.397 | 8.843 |
| D_{S_1} | 0.425 | 0.007 | 0.334 |
| D_{S_2} | 0.198 | 0.208 | 0.006 |
| D_{S_3} | 0.041 | 0.033 | 0.561 |
| D_{S_4} | 0.235 | 0.006 | 0.022 |
| D_{S_5} | 0.092 | 0.001 | 0.061 |
| D_{S_6} | 0.245 | 0.231 | 0.005 |

Table S1: Comparison of the experimentally observed ionization potentials $E_{IP}^?$ to the calculated vertical energies of the radical cation E_{IP}^{theo} at the ground state equilibrium structure of neutral tetracene, as well as the Dyson intensities D for transitions from different neutral states to the respective cationic state of tetracene.

S3.3 Calibration of the calculations

To verify the selection of our active space, we performed several CASSCF calculations including symmetry. We performed a 10 state-averaged CASSCF calculation with 12 and 14 active electrons and orbitals, respectively, as well as a 15 state-averaged CASSCF calculation with 16 active electrons and orbitals. In addition, an imaginary shift of $0.05 \text{ au}^?$ for the zero order Hamiltonian was included and the calculations were carried out using the ANO-L-VDZP basis set^{???}. The energies ΔE are calculated at CASPT2 level of theory and presented in table S2. The corresponding optimized molecular orbitals for the calculations with 12 and 14 active electrons and orbitals are shown in figure S5 and figure S6, respectively. The calculations described above were carried out using MOLCAS 8.4[?] and OpenMOLCAS v20.10[?].

The calculated energies of S_1 to S_6 differ by a maximum of $\sim 0.3 \text{ eV}$ (for S_4) between the different calculations, which shows an accurate selection of the active space. To further increase the accuracy of our calculations, we employed an active space of 16 active electrons and 16 active orbitals with a basis set of triple ζ quality ANO-L-VTZP^{???}. The energy

| state | $^1\Delta E$ / eV (sym.) | $^2\Delta E$ / eV (sym.) | $^3\Delta E$ / eV (sym.) |
|----------------|--------------------------|--------------------------|--------------------------|
| S ₁ | 2.85 (B _{2u}) | 3.04 (B _{2u}) | 2.83 (B _{2u}) |
| S ₂ | 3.52 (B _{3u}) | 3.52 (B _{3u}) | 3.48 (B _{3u}) |
| S ₃ | 3.79 (A _g) | 3.79 (A _g) | 3.88 (A _g) |
| S ₄ | 4.10 (B _{1g}) | 4.19 (B _{1g}) | 4.23 (B _{1g}) |
| S ₅ | 4.28 (B _{1g}) | 4.51 (B _{1g}) | 4.29 (B _{1g}) |
| S ₆ | 4.86 (B _{2u}) | 4.98 (B _{2u}) | 4.89 (B _{3u}) |

Table S2: Vertical excitation energies ΔE (in eV) of the six lowest-lying singlet states, calculated at the ground state equilibrium structure of tetracene. The symmetry of the state is indicated in parenthesis. ¹The results are obtained from a 10 state-averaged calculation per symmetry with 12 active orbitals and 12 active electrons. ²The results are obtained from a 10 state-averaged calculation per symmetry with 14 active orbitals and 14 active electrons. ³The results are obtained from a 15 state-averaged calculation per symmetry with 16 active orbitals and 16 active electrons.

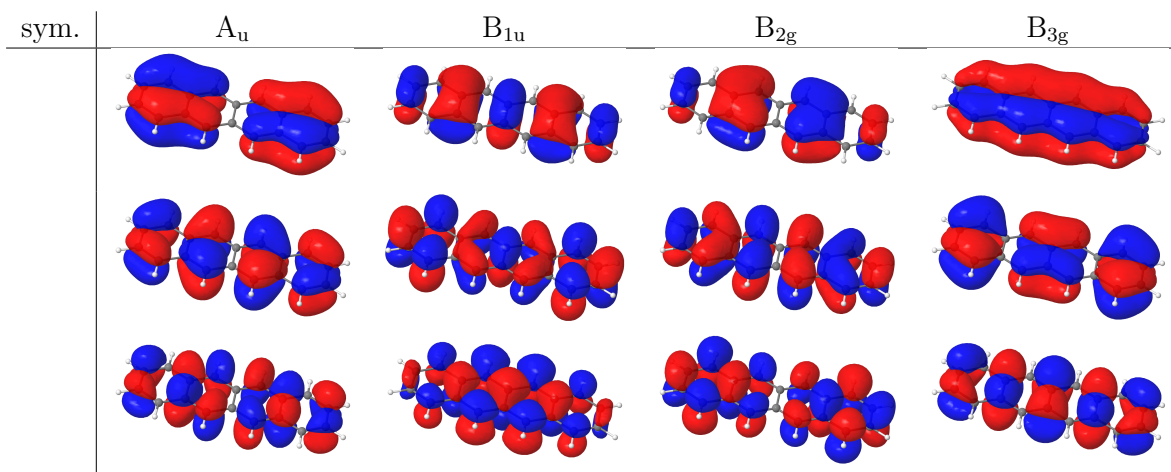


Figure S5: CASSCF optimized molecular orbitals and their corresponding symmetry. In the state-average calculations, 10 roots with 12 active orbitals and 12 active electrons were employed.

of S₁ decreased with the larger basis set reaching 2.75 eV, which differs from the experimental value[?] by only 0.02 eV. Overall, the relative energies of the singlet states are slightly smaller compared to the calculation with basis set ANO-L-VDZP and are presented in table 1.

S3.4 Geometries

The geometries were obtained using density functional theory (DFT) with the B3LYP exchange-correlation functional[?] and a def2-TZVP basis set[?]. For the relaxation, DFT-D3 dispersion interaction corrections[?] with Becke-Johnson damping[?] were employed. The optimized ground state equilibrium geometry (in Å) of the neutral tetracene and tetracene as a radical cation is provided in table S3 and table S4, respectively. The geometry optimizations were carried out using the Turbomole V7.5 package[?].

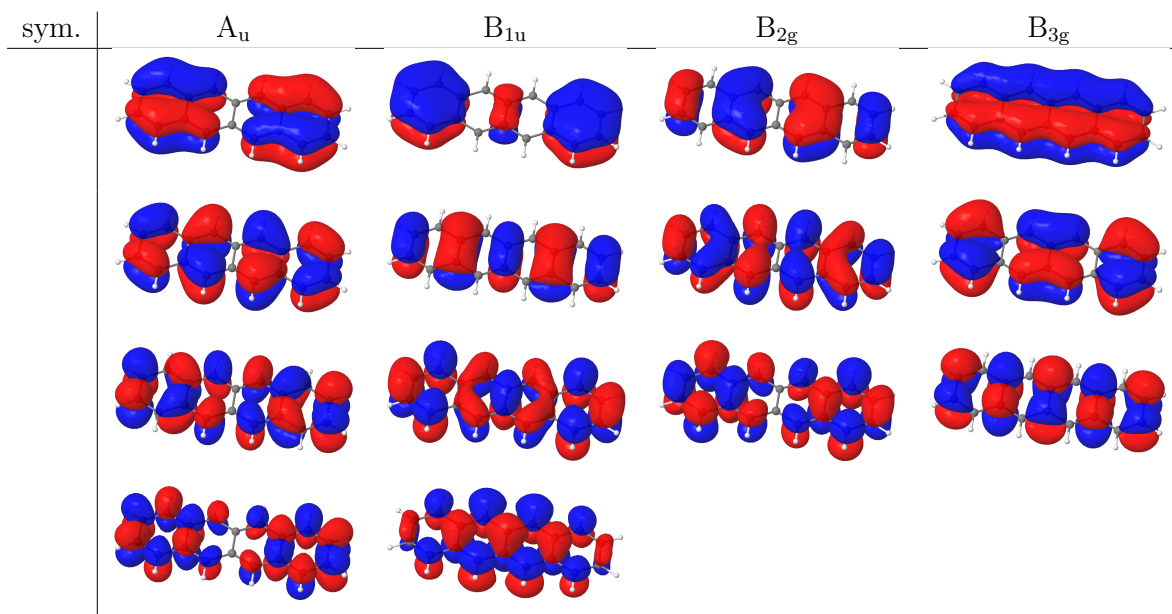


Figure S6: CASSCF optimized molecular orbitals and their corresponding symmetry. In the state-average calculations, 10 roots with 14 active orbitals and 14 active electrons were employed.

| atom | x | y | z |
|------|------------|------------|-----------|
| C | 2.4392170 | 0.7231002 | 0.0000000 |
| C | 1.2300798 | 1.4012461 | 0.0000000 |
| C | 0.0000000 | 0.7233739 | 0.0000000 |
| C | 0.0000000 | -0.7233739 | 0.0000000 |
| C | 1.2300798 | -1.4012461 | 0.0000000 |
| C | 2.4392170 | -0.7231002 | 0.0000000 |
| C | 3.6954713 | -1.4037934 | 0.0000000 |
| C | 4.8674639 | -0.7130534 | 0.0000000 |
| C | 4.8674639 | 0.7130534 | 0.0000000 |
| C | 3.6954713 | 1.4037934 | 0.0000000 |
| C | -1.2300798 | 1.4012461 | 0.0000000 |
| C | -2.4392170 | 0.7231002 | 0.0000000 |
| C | -2.4392170 | -0.7231002 | 0.0000000 |
| C | -1.2300798 | -1.4012461 | 0.0000000 |
| C | -3.6954713 | 1.4037934 | 0.0000000 |
| C | -4.8674639 | 0.7130534 | 0.0000000 |
| C | -4.8674639 | -0.7130534 | 0.0000000 |
| C | -3.6954713 | -1.4037934 | 0.0000000 |
| H | 1.2303876 | 2.4855248 | 0.0000000 |
| H | 1.2303876 | -2.4855248 | 0.0000000 |
| H | 3.6938585 | -2.4873222 | 0.0000000 |
| H | 3.6938585 | 2.4873222 | 0.0000000 |
| H | -1.2303876 | 2.4855248 | 0.0000000 |
| H | -1.2303876 | -2.4855248 | 0.0000000 |
| H | 5.8116057 | -1.2428699 | 0.0000000 |
| H | 5.8116057 | 1.2428699 | 0.0000000 |
| H | -3.6938585 | 2.4873222 | 0.0000000 |
| H | -5.8116057 | 1.2428699 | 0.0000000 |
| H | -5.8116057 | -1.2428699 | 0.0000000 |
| H | -3.6938585 | -2.4873222 | 0.0000000 |

Table S3: Cartesian coordinates of the equilibrium structure of the neutral tetracene (in Å).

| atom | x | y | z |
|------|------------|------------|-----------|
| C | 2.4462484 | 0.7195624 | 0.0000000 |
| C | 1.2234980 | 1.4030610 | 0.0000000 |
| C | 0.0000000 | 0.7228147 | 0.0000000 |
| C | 0.0000000 | -0.7228147 | 0.0000000 |
| C | 1.2234980 | -1.4030610 | 0.0000000 |
| C | 2.4462484 | -0.7195624 | 0.0000000 |
| C | 3.6824827 | -1.4037387 | 0.0000000 |
| C | 4.8670831 | -0.7042880 | 0.0000000 |
| C | 4.8670831 | 0.7042880 | 0.0000000 |
| C | 3.6824827 | 1.4037387 | 0.0000000 |
| C | -1.2234980 | 1.4030610 | 0.0000000 |
| C | -2.4462484 | 0.7195624 | 0.0000000 |
| C | -2.4462484 | -0.7195624 | 0.0000000 |
| C | -1.2234980 | -1.4030610 | 0.0000000 |
| C | -3.6824827 | 1.4037387 | 0.0000000 |
| C | -4.8670831 | 0.7042880 | 0.0000000 |
| C | -4.8670831 | -0.7042880 | 0.0000000 |
| C | -3.6824827 | -1.4037387 | 0.0000000 |
| H | 1.2254444 | 2.4867158 | 0.0000000 |
| H | 1.2254444 | -2.4867158 | 0.0000000 |
| H | 3.6853418 | -2.4862714 | 0.0000000 |
| H | 3.6853418 | 2.4862714 | 0.0000000 |
| H | -1.2254444 | 2.4867158 | 0.0000000 |
| H | -1.2254444 | -2.4867158 | 0.0000000 |
| H | 5.8085655 | -1.2371120 | 0.0000000 |
| H | 5.8085655 | 1.2371120 | 0.0000000 |
| H | -3.6853418 | 2.4862714 | 0.0000000 |
| H | -5.8085655 | 1.2371120 | 0.0000000 |
| H | -5.8085655 | -1.2371120 | 0.0000000 |
| H | -3.6853418 | -2.4862714 | 0.0000000 |

Table S4: Cartesian coordinates of the equilibrium structure of tetracene as a radical cation (in Å).